Bian et al. Nanoscale Research Letters (2017) 12:136
DOI 10.1186/s11671-017-1885-3

Nanoscale Research Letters

NANO EXPRESS Open Access

Enhanced Photovoltage Response of Hematite-X-Ferrite Interfaces (X = Cr, Mn, Co, or Ni)

Liang Bian[1,2,3*], Hai-long Li[2,3*], Yu-jin Li[3], Jia-nan Nie[3], Fa-qin Dong[2], Hai-liang Dong[4], Mian-xin Song[2], Li-sheng Wang[1], Tian-liang Zhou[1], Xiao-yan Zhang[2,3], Xin-xi Li[5] and Lei Xie[5]

Abstract

High-fluorescent p-X-ferrites (XFe_2O_4; XFO; X = Fe, Cr, Mn, Co, or Ni) embedded in n-hematite (Fe_2O_3) surfaces were successfully fabricated via a facile bio-approach using *Shewanella oneidensis* MR-1. The results revealed that the X ions with high/low work functions modify the unpaired spin Fe^{2+}–O^{2-} orbitals in the XFe_2O_4 lattices to become localized paired spin orbitals at the bottom of conduction band, separating the photovoltage response signals (73.36~455.16/−72.63~−32.43 meV). These (Fe_2O_3)–O–O–(XFe_2O_4) interfacial coupling behaviors at two fluorescence emission peaks (785/795 nm) are explained via calculating electron-hole effective masses (Fe_2O_3–$FeFe_2O_4$ 17.23×10^{-31} kg; Fe_2O_3–$CoFe_2O_4$ 3.93×10^{-31} kg; Fe_2O_3–$NiFe_2O_4$ 11.59×10^{-31} kg; Fe_2O_3–$CrFe_2O_4$ -4.2×10^{-31} kg; Fe_2O_3–$MnFe_2O_4$ -11.73×10^{-31} kg). Such a system could open up a new idea in the design of photovoltage response biosensors.

Keywords: Heterostructure, Fluorescence enhancement, Quantum dots, *Shewanella oneidensis* MR-1

Background

As a n-type semiconductor, hematite (Fe_2O_3) is an important semiconductor in the fields of photoluminescence and electron paramagnetic imaging due to its chemical stability and band gap (2 eV) [1]. However, poor minority charge carrier mobility (0.2 $cm^2\ V^{-1}\ s^{-1}$) and ultrafast recombination of photogenerated carriers (~10 ps) limit its application as a high-photostability fluorescent material [2]. Recently, an interesting option is the conjugation of Fe_2O_3 with a p-type ferrite (band gaps 1.9~2.7 eV) with a lower but similar conduction band level and an appropriate valence band level [3]. It has two advantages, e.g., unpaired-paired spin change and electron-hole recombination [4]. For example, Sun et al. [5] confirmed that the electrons flow through the energy barrier between the Fe_2O_3 and Fe_3O_4 phases, according to spin-dependent tunneling mode. Higher void fraction of cubic Fe_3O_4 provides more transfer channels for tetrahedral ion diffusion and charge transfer. To enhance separation rate of photoinduced charge carriers, Shen et al. [6] used Mg to modify the surface photovoltage of Fe_3O_4/Fe_2O_3 heterostructured hollow nanospheres. A remarkable surface photovoltage response in UV and visible spectral region (320~570 nm) was attributed to the $2p(O^{2-})\rightarrow3d(Fe^{3+})$ charge transfer and $Fe^{3+}(3d_5)$ crystal field transitions of the $MgFe_2O_4$ and Fe_2O_3 interface. Therefore, the incorporation of the magnetic nanocrystals associated with heavy metal ion (X)-modified Fe_3O_4 on the Fe_2O_3 surface can not only improve fluorescence intensity but also recycle the fluorescence by magnetic separation under modest magnetic fields [7].

In the present work, we designed a facile approach to reduce the effect of lattice mismatch of the components, for coating directly p-ferrite on the n-hematite using *Shewanella oneidensis* MR-1 [8]. Therein, the cytochromes (OmcA, MtrC, and MtrB) and periplasmic [Fe] hydrogenases of the extracellular matrix represent the bio-reactions as follows: $lactate^- + 4Fe^{3+} + 2H_2O \rightarrow acetat^- + HCO^- + 4Fe^{2+} + 5H^+$ [9]; $X^{2+} + 2Fe(OH)_3$

* Correspondence: bianliang555551@126.com; well09131015@126.com
[1]Institute of Gem and Material Technology, Hebei GEO University, Shijiazhuang 050000, Hebei, China
[2]Key Laboratory of Solid Waste Treatment and Resource Recycle, Ministry of Education, South West University of Science and Technology, Mianyang 621010, Sichuan, China
Full list of author information is available at the end of the article

$\rightarrow XFe_2O_4 + 2H_2O + 2H^+$ [10]. Therefore, XFe_2O_4 particles will be directly formed from the Fe_2O_3 surface, creating a Fe_2O_3–XFe_2O_4 interface. The purpose of this paper is to enhance both surface photovoltage response and fluorescence, for designing new multifunctional sensor.

Methods

Here, *S. oneidensis* MR-1 was cultured in a chemically defined minimal medium as described previously [11]. MR-1 cells were cultured aerobically on TSB (without dextrose) for 16 h at 30 °C with shaking at 100 rpm. Cells were washed twice and centrifuged at 6000 rpm for 10 min in sterile PIPES/AQDS buffer at pH 7, followed by one wash and re-suspension to ~10^9 cells ml^{-1} in M1 medium. Anaerobically grown cells of MR-1 were added to the tubes containing the magnetite and M1 medium to obtain a final concentration of 2.3×10^8 cells ml^{-1}. The total volume of medium in each tube, including X(Cr, Mn, Co, or Ni)-modified goethite (FeOOH) and cells, was 250 ml. The X-modified Fe_3O_4 in the medium had a final concentration of 90 mM [12]. All treatment tubes were incubated in the dark at 30 °C until the end of the experiment. All treatments with anaerobically cultured cells were incubated for 45 days.

The size of the laser spot was less than 2 μm, and the acquisition time for all spectra was 20 s. Scanning electron microscopy (SEM) and energy-dispersive X-ray spectroscopy (EDS) were performed on a Cu plate with a Hitachi S-4800 field emission machine with an accelerating voltage of 5 KeV [13]. The X-ray diffraction data were collected for all Fe_2O_3–XFe_2O_4 heterostructures using an X-ray diffractometer (Bryke D8-Advance, Germany, Cu K_α radiation, $\lambda = 0.154$ nm, 40 kV, 40 mA) [14]. Raman scattering measurements (Labram HR evolution, Horiba Scientific, France) were conducted at room temperature under a backscattering geometric configuration using a WITec-Alpha confocal micro-Raman system [15]. The light absorption properties of the heterostructures were tested by UV-Vis diffuse reflectance spectroscopy (DRS) (Evolution 220, USA) [16]. Atomic force microscope (AFM) and Kelvin probe force microscopy (KPFM) measurements were performed on an atomic force microscope (Asylum Research MFP-3D, USA) [17]. Photoluminescence (PL) emission at room temperature was obtained at 420~900 nm with an excitation wavelength at 400 nm. The slit widths for both the excitation and emission were 5.0 nm. A fiber-based fluorescence spectrometer (USB 4000, Ocean Optics, USA) was used to record the in situ PL spectra [18].

Besides, we simulated the effective masses of electron-hole pairs, dielectric functions (ε), and spin-partial densities of states (spin-PDOSs) via Kramers-Kronig transform to give an insight into the electron transfer process at the atomic level and to contribute to the interpretation of experimental results from techniques such as DRS, KPFM-AFM, or PL, based on the generalized gradient-corrected Perdew-Burke-Ernzerhof functional + U (GGA-PBE) (Castep, Materials studio, Accelrys, USA) [19], where the Coulomb and screened exchange parameters (U, J) were set 5 and 1 eV, respectively. A kinetic energy cutoff of 300 eV for the electrons was used, well within the convergence of a total-energy calculation. A $2 \times 2 \times 2$ super cell was introduced for the interstitial plane-wave, and a $5 \times 5 \times 5$ k-point mesh for integration over the Brillouin zone.

Results and Discussion

Structural Characterization

In Burns' opinion [20], the reduced Fe^{2+} precipitates tend to accumulate on the extracellular polymeric substance cytochrome and [Fe] hydrogenases of *S. oneidensis* MR-1, forming the Fe_3O_4 phase. And H^+ ions as the electron donors at pH6 can mediate the electron transfer between Fe^{2+} and X^{2+} to modify the Fe_3O_4 surface. Figure 1a confirms that X-modified Fe_3O_4 and Fe_2O_3 are coexisting, because the 500-nm rice-like Fe_3O_4 particles are attached onto the 3.5-μm Fe_2O_3 surfaces. And total mass ratios of Fe, O, and X are 26.66~57.98 wt.%, 43.61~46.65 wt.%, and 8.36~11.89 wt.%, respectively.

To verify the crystalline structure of the as-synthesized sample, typical power XRD patterns are shown in Fig. 1b. The clear diffraction peaks at 2θ angles (approximately 27°, 35.5°, 47°, 30.5°, 39°, 53.5°, 57.5°) can be assigned to the (012), (311), and (110) characteristic reflections of Fe_2O_3 (JCPDS 89-5892) and the (311), (222), (422), and (511) characteristic reflections of the cubic structure of magnetite XFe_2O_4 (JCPDS 19-0629) [21, 22]. The narrow and sharp peaks suggest that the obtained XFe_2O_4 and Fe_2O_3 are highly crystalline in nature, with average crystallite sizes approximately 41.32~44.21 nm and 28.78~32.79 nm at the Fe_2O_3–(012) and XFO–(311) planes, respectively.

To further identify the interactions of iron oxides, we used lines in Fig. 1c to depict the typical Raman spectrum of Fe_2O_3–XFe_2O_4 heterostructures. The Raman band at the F_{2g}, E_g, and E_{2g} modes reflect translational movement of the tetrahedron, symmetric bending of oxygen with respect to the metal ion, and asymmetric stretching of Fe(X) and O, respectively. These bands reflect that Fe_2O_3 comprises hexagonal close-packed layers of O^{2-} and that Fe^{3+} ions fill two thirds of the octahedral voids, forming a FeO_6 octahedral layer. XFe_2O_4 is a normal spinel, with X^{2+} ions at tetrahedral sites and Fe^{3+} ions at octahedral sites. On another side, we can see that a broad asymmetric D peak at 915~970 cm^{-1} as the phonon scattering near the Brillouin zone boundary is

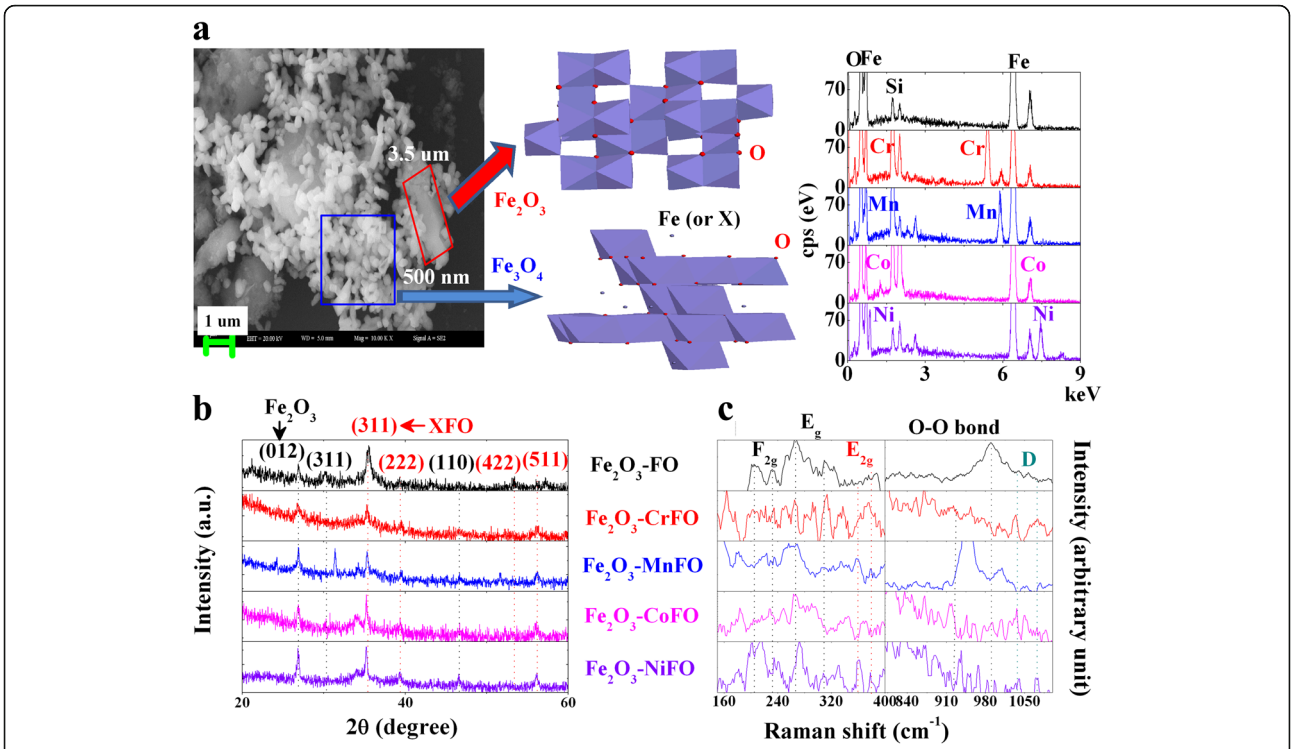

Fig. 1 **a** SEM image of Fe_2O_3–Fe_3O_4 and EDS-SEM patterns of Fe_2O_3–XFe_2O_4. **b**, **c** show the relative XRD and Raman patterns

attributed to the long-range (Fe_2O_3)–O–O–(XFe_2O_4) interface. These results confirm that the surface Fe_2O_3 has been successfully reduced as a XFe_2O_4 and that they are bonded to each other with the shared oxygen atoms of the octahedron-tetrahedron.

Unpaired-Paired Spin Change in the Lattice

In the literature [3], the enhanced photovoltage response performances can be attributed to intra- or inter-electronic transition in the UV and visible region. The origin of electron transfer enhancement of Fe_2O_3–XFe_2O_4 can be summarized by (i) unpaired-paired spin change in the lattice and (ii) electron-hole recombination in the interface. Figure 2a verifies that the X ions enhance the average fluorescence intensities by 3.13~6.35 multiples than that of Fe_2O_3–Fe_3O_4, where the band gap differences in Fig. 2b are close to the Fermi point, providing high electron transfer ratios. In the octahedral Fe^{3+}–O^{2-} orbital at an intrinsic main fluorescence emission peak of 390 nm, the absorption bands can be attributed to two charge transfers as the oxygen-to-metal $2p(O^{2-})\rightarrow 3d(Fe^{3+})$ (left region: Fe_2O_3; and middle region: XFe_2O_4) intra-atomic transitions, reflecting the non-degeneracy ($^6A_1$)→three orbital degeneracy (T_{2g}) inter-atomic transition [23]. This corresponds to the T_{2g}–T_{2g} orbital degeneracy, as shown in Fig. 2c.

On another side, the spin parity of the iron pairs can remain the same in the excited state, showing the spin-down PDOSs. To modify the electron transfer behaviors in tetrahedral Fe^{2+}–O^{2-} orbitals at two broad blue fluorescence emission peaks at 450 and 473 nm, we used X^{2+} as an acceptor to occupy the tetrahedral sites at the bottom of the conduction band, and thus, the electronic transitions implying Fe^{2+}(or X^{2+})–O^{2-} orbitals are known to be only at the origin of charge transfers between the bottom of the conduction band and the top of the valence band. The unpaired spin orbitals change into paired spin orbitals; therefore, the paired spin orbitals enhance the spin quantum number (S) to 1, changing the multiplicity of the excited state ($M = 2S + 1$) into 3. This unpaired-paired spin change provides more active electron gas in the Fe_2O_3–XFe_2O_4 interface to enhance the average luminous intensities as 3.31~8.18 multiples than that of Fe_2O_3–Fe_3O_4 by the excitation of 488 nm, as presented in Fig. 3a. The accelerated electron-hole recombination [24] at the near-infrared photoresponse region is beneficial for transferring long-range electrons to separate the photovoltage response signal.

Electron-Hole Recombination in the Interface

Ultimately, we found that Fe_3O_4 has a significant photovoltage response red shifted to 257.7 meV from

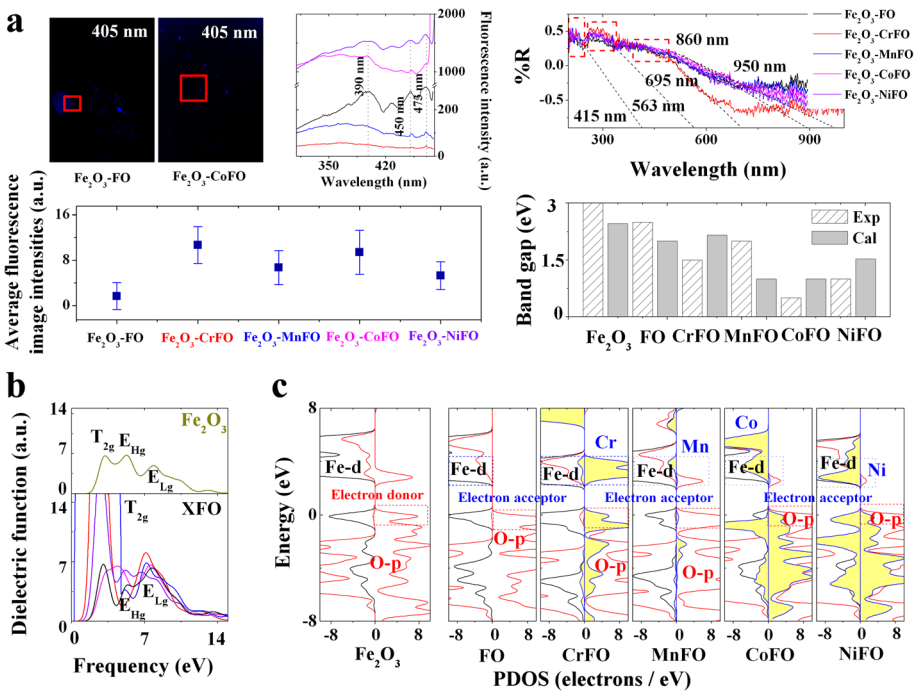

Fig. 2 **a** Fluorescence images, average luminous intensities, and PL patterns of Fe_2O_3–XFe_2O_4 by the excitation of 405 nm. **b** reflects the DRS patterns and confrontation between experimental and calculated band gaps of Fe_2O_3–XFe_2O_4. The absorption bands were tested through the slopes of diffuse reflectance curves that the experimental and calculated band gaps are similar with each other. **c** shows the calculated dielectric functions and spin-PDOSs of Fe_2O_3–XFe_2O_4

those of Fe_2O_3 in Fig. 3b, which allows for the efficient separation of electron-hole pairs at the Fe_2O_3–Fe_3O_4 interface, which will be higher than that (200 meV) of the reported Fe_2O_3–$ZnFe_2O_4$ interface [25–27]. The origin of the high/low photovoltage response region (theoretical difference data ~200 meV; experimental difference data 45~160 meV) is attributed to the surface potential difference (270 meV/3~70 meV) of Fe_2O_3 and XFe_2O_4, according to the theoretical potential images (see Fig. 3c). The photovoltage response signal in the low photovoltage response region is modified via the X–Fe–O orbital degeneracy.

To our knowledge, the crystal field theory indicates that the Fe–d orbital will split into the doubly degenerate e_g orbital (d_{z2} and d_{x2-y2}) and triple degenerate t_{2g} orbital (d_{xy}, d_{yz}, and d_{xz}) [28]. On the one hand, the high-energy Fe–d_{x2-y2} orbital (work function 4.5 eV) can be modified by the X–d_{x2-y2} orbital with the higher work functions (Co 4.7 eV and Ni 4.6 eV) [29]. The X ions reduce both octahedral and tetrahedral surface potentials (~0.7 and 10 meV); because of that, the down-spin Co^{2+} (or Ni^{2+})–Fe^{3+} interfacial coupling degenerates with the down-spin d_{x2-y2} orbital of Fe^{2+}–$3d^64s^2$ (Fig. 2c) at the high-energy e_{Hg} orbital. It not only enhances the positive potential direction (polarization angle 5~15° → 60~100°) but also accelerates the electron-hole recombination to create a highly effective mass hole (Fe_2O_3–$FeFe_2O_4$ 17.23×10^{-31} kg; Fe_2O_3–$CoFe_2O_4$ 3.93×10^{-31} kg; Fe_2O_3–$NiFe_2O_4$ 11.59×10^{-31} kg) (see Fig. 3d). A responsibility of the intrinsic main fluorescence emission peak blue shifts to 785 nm.

On the other hand, the Fe–O d_{z2}–p_{z2} orbital is being modified by the X-d_{z2} orbital with lower work functions (Cr 4.41 eV and Mn 4.1 eV). The data curve showed that the d_{z2}–d_{z2}–p_{z2} orbital degeneracy creates a weak quantum well of oxygen vacancy for long-range electronic transition at the low-energy doubly degenerate e_{Lg} orbital. A part of O–$2p^4$ electron is trapped in the oxygen vacancy with the deep holes present in the valence band, according to the enhanced electron effective mass (Fe_2O_3–$CrFe_2O_4$ -4.2×10^{-31} kg; Fe_2O_3–$MnFe_2O_4$ -11.73×10^{-31} kg). The down-spin p_{z2} orbital changes its direction to become an up-spin orbital, showing the negative photovoltage response signal (Cr −32.43 meV; Mn −72.63 meV). Consequently, the different photovoltage response behaviors above can be used for the design of high-mobility electronic devices and fluorescent probes for different heavy metal ion imaging, oxygen evolution catalysts [30], and biomolecules [31], etc.

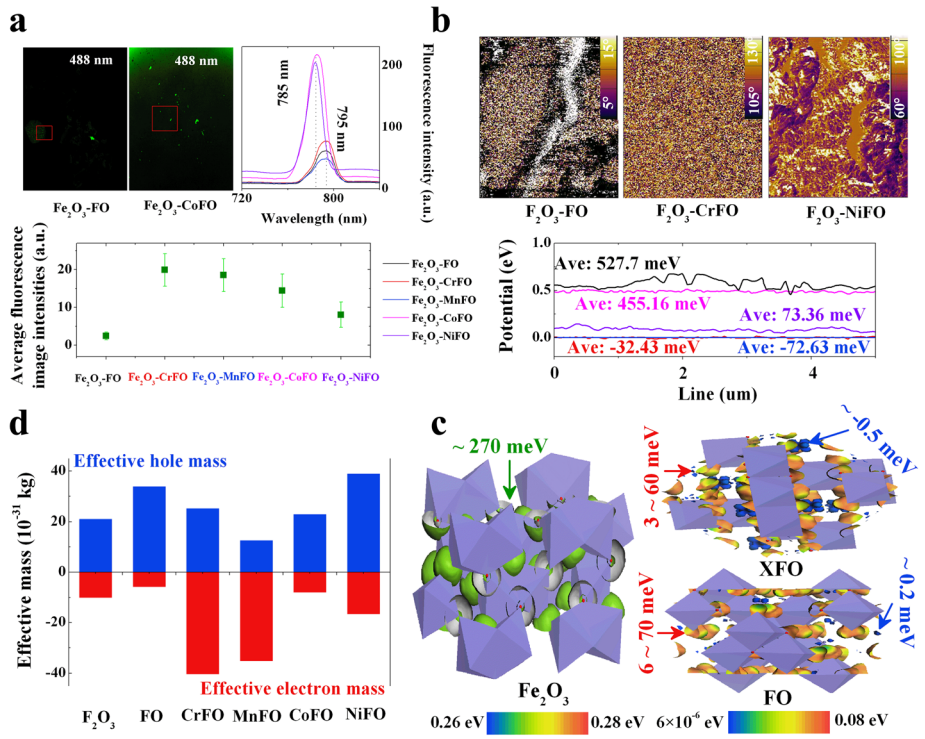

Fig. 3 **a** Fluorescence images, average luminous intensities, and PL patterns of Fe_2O_3–XFe_2O_4 by the excitation of 488 nm. **b** reflects the surface photovoltages and KPFM phase images. The work function values of Fe_2O_3 and $FeFe_2O_4$ are 5.35 eV [26] and 5.52 eV [27], respectively, and the charges transfer between the different work functions of two materials for their Fermi levels to equilibrate. The corresponding theoretical surface potential images are shown in (**c**). **d** means the calculated effective masses of electron-hole pairs and surface potential illustration

Conclusions

In summary, a novel bio-induced phase transition method for the growth of XFe_2O_4 embedded in a Fe_2O_3 is proposed here using *S. oneidensis* MR-1. We explained the mechanism of surface photovoltage response and high-photostability fluorescence. The present work demonstrates that the calculated unpaired-paired spin X^{2+}–Fe^{2+}–O_2- orbitals verify the enhanced photovoltage response signal (theoretical data ~200 meV; experimental data 45~160 meV) and separate the high/low surface potential regions (270 meV/3~70 meV) based on the calculated electron-hole effective masses. As a consequence, our works provide a reference for designing new photoluminescence and electron paramagnetic imaging biosensors. Further investigation will be focused on the electron transfer process between interfaces and heavy metal ions in an aquatic environment to garner a better understanding of the selective fluorescence probe application.

Acknowledgements

The authors acknowledge the financial supports by the 973 project (2014CB8460003), the One-Thousand-Talents Scheme in Sichuan Province, Xinjiang Science Fund of Outstanding Young Scholars (qn2015yx034), Hebei outstanding young scholars, Science and Technology Program of Hebei Province (D2016403064 and 16044601Z), and Hebei Science and Technology Support Program (15211121).

Authors' Contributions

LB draft the manuscript and with FD, HD, and MS designed the experimental synthesis and theoretical simulation of XFO-BFO. HL participated in the experimental and theoretical design, FD in the spectrum measurement and analysis. YL and JN directed the experiment on the synthesis of XFO-BFO by microorganism method. LW, TZ, and XZ participated in the microbial synthesis experiment. XL and LX carried out modifying the XFO-BFO by doping the Cr, Mn, Co, or Ni, and the SEM characterization. All authors read and approved the final manuscript.

Competing Interests

The authors declare that they have no competing interests.

Author details

[1]Institute of Gem and Material Technology, Hebei GEO University, Shijiazhuang 050000, Hebei, China. [2]Key Laboratory of Solid Waste Treatment and Resource Recycle, Ministry of Education, South West University of Science and Technology, Mianyang 621010, Sichuan, China. [3]Key Laboratory of Functional Materials and Devices under Special Environments, Chinese Academy of Sciences, Urumqi 830011, Xinjiang, China. [4]Department of Geology and Environmental Earth Science, Miami University, Oxford 45056, OH, USA. [5]Institute of Nuclear Physics and Chemistry, CAEP, Mianyang 621900, Sichuan, China.

Received: 12 December 2016 Accepted: 31 January 2017
Published online: 21 February 2017

References

1. Teleki A, Suter M, Kidambi PR, Ergeneman O, Krumeich F, Nelson BJ, Pratsinis SE (2009) Hermetically coated superparamagnetic Fe_2O_3 particles with SiO_2 nanofilms. Chem Mater 21:2094–2100
2. Sivula K, Zboril R, Formal FL, Robert R, Weidenkaff A, Tucek J, Frydrych J, Grätzel M (2010) Photoelectrochemical water splitting with mesoporous

hematite prepared by a solution-based colloidal approach. J Am Chem Soc 132:7436–7444
3. Pailhe' N, Wattiaux A, Gaudon M, Demourgues A (2008) Correlation between structural features and vis–NIR spectra of α-Fe_2O_3 hematite and AFe_2O_4 spinel oxides (A = Mg, Zn). J Solid State Chem 181:1040–1047
4. Ren Y, Wang J, Huang X, Ding J (2016) Enhanced lithium-ion storage performance by structural phase transition from two-dimensional rhombohedral Fe_2O_3 to cubic Fe_3O_4. Electrochim Acta 198:22–31
5. Sun AC, Kuo PC, Chou CY, Chen SC, Lie CT, Lin MH, Chen JW, Huang HL (2004) Magnetoresistance of sintered $(Fe_2O_3)_{1.00-x}(Fe_3O_4)_x$ ferrites. J Magnetism Magnetic Mater 272–276:1776–1777
6. Shen Y, Zhao Q, Li X, Hou Y, Chen G (2012) Surface photovoltage property of magnesium ferrite/hematite heterostructured hollow nanospheres prepared with one-pot strategy. Colloid Sur A: Physicochem Engin Aspects 403:35–40
7. Yang L, Jin R, Liang Y, Wang F, Yin P, Yi C (2015) Preparation and magnetic properties of $NiFe_2O_4$–Fe_2O_3@SnO_2 heterostructures. Mater Lett 153:55–58
8. Lower SK, Hochella MF, Beveridge TJ (2001) Bacterial recognition of mineral surfaces: nanoscale interactions between shewanella and α-FeOOH. Sci 292:1360–1363
9. Ma S, Banfield JF (2011) Micron-scale Fe^{2+}/Fe^{3+}, intermediate sulfur species and O_2 gradients across the biofilm-solution-sediment interface control biofilm organization. Geochim Cosmochim Acta 75:3568–3580
10. Burgos WD, McDonough JT, Senko JM, Zhang G, Dohnalkova AC, Kelly SD, Gorby YA, Kemner KM (2008) Characterization of uraninite nanoparticles produced by Shewanella oneidensis MR-1. Geochim Cosmochim Acta 72:4901–4915
11. Zhang G, Burgos WD, Senko JM, Bishop ME, Dong H, Boyanov MI, Kemner KM (2011) Microbial reduction of chlorite and uranium followed by air oxidation. Chem Geol 283:242–250
12. Bian L, Li H, Dong H, Dong F, Song M, Wang L, Zhou T, Li W, Hou W, Zhang X, Lu X, Li X, Xie L (2017) Fluorescent enhancement of bio-synthesized X-Zn-ferrite-bismuth ferrite (X=Mg, Mn or Ni) membranes: experiment and theory. Appl Sur Sci 396:1177–1186
13. Bamoniri A, Moshtael-Arani N (2015) Nano-Fe_3O_4 encapsulated-silica supported boron trifluoride as a novel heterogeneous solid acid for solvent-free synthesis of arylazo-1-naphthol derivatives. RSC Adv 5:16911–16920
14. Li J, Hu Y, Yang J, Wei P, Sun W, Shen M, Zhang G, Shi X (2015) Hyaluronic acid-modified Fe_3O_4@Au core/shell nanostars for multimodal imaging and photothermal therapy of tumors. Biomater 38:10–21
15. Seo SH, Kim BM, Joe A, Han HW, Chen X, Cheng Z, Janga ES (2014) NIR-light-induced surface-enhanced Raman scattering for detection and photothermal/photodynamic therapy of cancer cells using methylene blue-embedded gold nanorod@SiO_2 nanocomposites. Biomater 35:3309–3318
16. Bian L, Dong H, Dong F, Song M, Li H, Hou W, Zhang X, Wang L, Sun G, Li X, Xie L (2016) Mechanism of fluorescence enhancement of bio-synthesized XFe_2O_4-$BiFeO_3$ (X = Cr, Mn, Co or Ni) membranes. Nanoscale Res Lett 11:543–550
17. Zhao P, Bian L, Wang L, Xu J, Chang A (2014) Enhanced open voltage of $BiFeO_3$ polycrystalline film by surface modification of organolead halide perovskite. Appl Phys Lett 105:013901–013903
18. Li J, Huang Z, Wu D, Yin G, Liao X, Gu J, Han D (2010) Preparation and protein detection of Zn-Ferrite film with magnetic and photoluminescence properties. J Phys Chem C 114:1586–1592
19. Bian L, Xu J, Song M, Dong H, Dong F (2013) Effects of halogen substitutes on the electronic and magnetic properties of $BiFeO_3$. RSC Adv 3:25129–25135
20. Burns JL, Ginn BR, Bates DJ, Dublin SN, Taylor JV, Apkarian RP, Amaro-Garcia S, Neal AL, DiChristina TJ (2010) Outer membrane-associated serine protease involved in adhesion of Shewanella oneidensis to Fe(III) oxides. Envir Sci Techn 44:68–73
21. Sa T, Wu G, Qin N, Bao D (2012) Solution processed highly sensitive visible-light photodetectors based on α-Fe_2O_3/p-Si heterojunctions. Sen Act B: Chem 173:414–418
22. Horák D, Shagotova T, Mitina N, Trchová M, Boiko N, Babič M, Stoika R, Kovářová J, Hevus O, Beneš MJ, Klyuchivska O, Holler P, Zaichenko A (2011) Surface-initiated polymerization of 2-hydroxyethyl methacrylate from heterotelechelic oligoperoxide-coated γ-Fe_2O_3 nanoparticles and their engulfment by mammalian cells. Chem Mater 23:2637–2649
23. Todol JL, Mermet JM (2006) Sample introduction systems for the analysis of liquid microsamples by ICP-AES and ICP-MS. Spectrochim Acta B 61:239–283
24. Chen YZ, Bovet N, Trier F, Christensen DV, Qu FM, Andersen NH, Kasama T, Zhang W, Giraud R, Dufouleur J, Jespersen TS, Sun JR, Smith A, Nygård J, Lu L, Büchner B, Shen BG, Linderoth S, Pryds N (2013) A high-mobility two-dimensional electron gas at the spinel/perovskite interface of γ-Al_2O_3/$SrTiO_3$. Nat Comm 4:1371–1375
25. McDonald KJ, Choi KS (2011) Synthesis and photoelectrochemical properties of Fe_2O_3/$ZnFe_2O_4$ composite photoanodes for use in solar water oxidation. Chem Mater 23:4863–4869
26. Fan Z, Wen X, Yang S, Lu JG (2005) Controlled p- and n-type doping of Fe_2O_3 nanobelt field effect transistors. Appl Phys Lett 87:013113–013115
27. Wang C, Daimon H, Sun S (2009) Dumbbell-like Pt–Fe_3O_4 nanoparticles and their enhanced catalysis for oxygen reduction reaction. Nano Lett 9:1493–1496
28. Mi WB, Jiang EY, Bai HL (2009) Current-perpendicular-to-plane transport properties of polycrystalline Fe_3O_4/α-Fe_2O_3 heterostructures. Appl Phys Lett 93:132504–132507
29. Muñoz AG, Staikov G (2006) Electrodeposition of Co on oxide modified p-Si surfaces. Electrochim Acta 51:2836–2844
30. Peng X, Du J, Fan J, Wang J, Wu Y, Zhao J, Sun S, Xu T (2007) A selective fluorescent sensor for imaging Cd2+ in living cells. J Am Chem Soc 129: 1500–1501
31. Bian L, Dong F, Song M, Xu J, Zhang X (2015) Computational study of the cation-modified GSH peptide interactions with perovskite-type BFO-(111) membranes under aqueous conditions. Nanoscale Res Lett 10:261–267